

Sn-Doping Enhanced Ultrahigh Mobility $\text{In}_{1-x}\text{Sn}_x\text{Se}$ Phototransistor

Christy Roshini Paul Inbaraj,^{†,‡,§,||} Vijay Kumar Gudelli,^{||} Roshan Jesus Mathew,^{†,‡,⊥,||} Rajesh Kumar Ulaganathan,^{#,||} Raman Sankar,^{#,¶,||} Hsia Yu Lin,^{§,||} Hung-I Lin,^{§,||} Yu-Ming Liao,^{‡,§,||} Hao-Yu Cheng,^{¶,||} Kung-Hsuan Lin,^{¶,||} Fang Cheng Chou,[#] Yit-Tsong Chen,^{⊥,∇,||} Chih-Hao Lee,[†] Guang-Yu Guo,^{§,||} and Yang-Fang Chen^{*,§,⊙}

[†]Department of Engineering and System Science, National Tsing Hua University, Hsinchu 30013, Taiwan

[‡]Nano-Science and Technology Program, Taiwan International Graduate Program, and [¶]Institute of Physics, Academia Sinica, Taipei 11529, Taiwan

[§]Department of Physics, [#]Center for Condensed Matter Sciences, [∇]Department of Chemistry, and [⊙]Advanced Research Centre for Green Materials Science and Technology, National Taiwan University, Taipei 10617, Taiwan

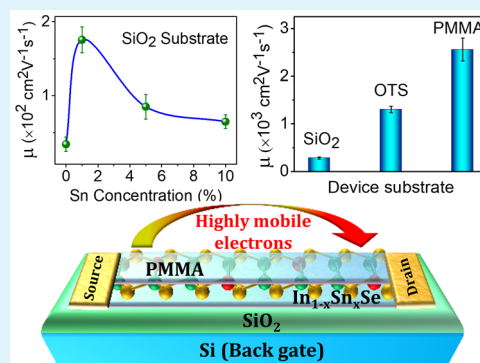
^{||}Physics Division, National Center for Theoretical Sciences, Hsinchu 30013, Taiwan

[⊥]Institute of Atomic and Molecular Sciences, Academia Sinica, Taipei 10617, Taiwan

S Supporting Information

ABSTRACT: Two-dimensional ternary materials are attracting widespread interest because of the additional degree of freedom available to tailor the material property for a specific application. An $\text{In}_{1-x}\text{Sn}_x\text{Se}$ phototransistor possessing tunable ultrahigh mobility by Sn-doping engineering is demonstrated in this study. A striking feature of $\text{In}_{1-x}\text{Sn}_x\text{Se}$ flakes is the reduction in the oxide phase compared to undoped InSe, which is validated by spectroscopic analyses. Moreover, first-principles density functional calculations performed for the $\text{In}_{1-x}\text{Sn}_x\text{Se}$ crystal system reveal the same effective mass when doped with Sn atoms. Hence, because of an increased lifetime owing to the enhanced crystal quality, the carriers in $\text{In}_{1-x}\text{Sn}_x\text{Se}$ have higher mobility than in InSe. The internally boosted electrical properties of $\text{In}_{1-x}\text{Sn}_x\text{Se}$ exhibit ultrahigh mobility of $2560 \pm 240 \text{ cm}^2 \text{ V}^{-1} \text{ s}^{-1}$ by suppressing the interfacial traps with substrate modification and channel encapsulation. As a phototransistor, the ultrathin $\text{In}_{1-x}\text{Sn}_x\text{Se}$ flakes are highly sensitive with a detectivity of 10^{14} Jones. It possesses a large photoresponsivity and photogain ($V_g = 40 \text{ V}$) as high as $3 \times 10^5 \text{ A W}^{-1}$ and 0.5×10^6 , respectively. The obtained results outperform all previously reported performances of InSe-based devices. Thus, the doping-engineered $\text{In}_{1-x}\text{Sn}_x\text{Se}$ -layered semiconductor finds a potential application in optoelectronics and meets the demand for faster electronic technology.

KEYWORDS: high-mobility, responsivity, phototransistor, indium selenide, 2D materials



INTRODUCTION

The field-effect phototransistors using two-dimensional (2D) materials are revolutionizing the field of optoelectronics in recent years. It began with the discovery of graphene, a monolayer form of graphite, which initiated great anticipation among the researchers to supersede the silicon-based electronics because of their intriguing electronic and mechanical properties.^{1,2} Though graphene was reported to have high carrier mobility as the electrons behave as massless Dirac fermions, the lack of band gap limited their usage in phototransistors.³ This limitation routed by transition-metal dichalcogenides (TMD) which possess a sizable band gap along with excellent electronic properties advanced 2D material-based optoelectronic fields.^{4,5} Among the TMDs, MoS_2 , WS_2 , and WSe_2 have been widely studied by researchers.^{5–8} Although they exhibit a high photoresponse, their mobility remains low because of their large carrier

effective mass. Despite several attempts like using a high k dielectric for top-gating and encapsulating MoS_2 , reducing the barrier height, and suppressing the interfacial impurities to enhance the mobility of MoS_2 , the maximum mobility of MoS_2 reported is $\sim 500 \text{ cm}^2 \text{ V}^{-1} \text{ s}^{-1}$.^{9–14} Alternatively, black phosphorus has grasped the attention with a high mobility of about $1000 \text{ cm}^2 \text{ V}^{-1} \text{ s}^{-1}$ but its highly unstable nature is a major drawback.¹⁵ Hence, in recent years, there has been growing interest in group III monochalcogenide InSe because of its low electron effective mass ($m_{\perp} = 0.131m_0$, $m_{\parallel} = 0.081m_0$)¹⁶ which results in high mobility.

The first study on a few-layered InSe phototransistor by Tamalampudi et al. reported mobility of about $0.1 \text{ cm}^2 \text{ V}^{-1} \text{ s}^{-1}$

Received: April 12, 2019

Accepted: June 17, 2019

Published: June 17, 2019



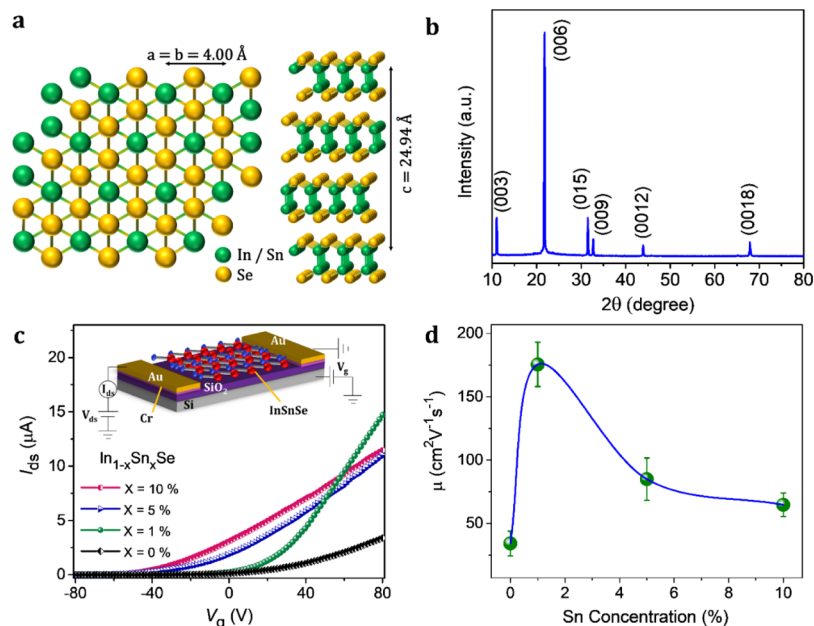


Figure 1. Characterization of the few-layered InSnSe crystals. (a) Crystal structure of the as-grown InSnSe single crystal. (b) X-ray diffraction pattern of the InSnSe crystal. (c) I_{ds} - V_g characteristic curves measured by scanning V_g from -80 to 80 V at $V_{ds} = 0.1$ V for different concentrations of Sn in the $In_{1-x}Sn_xSe$ crystal. The inset represents the schematic of the InSnSe field effect transistor. (d) The plot depicts the estimated mobility as a function of Sn concentration in the $In_{1-x}Sn_xSe$ crystal.

on an SiO_2/Si substrate.¹⁷ Subsequently, Feng et al. and Sucharitakul et al. tried to reduce the carrier scattering because of the Coulomb impurities at the interface and achieved a room temperature mobility of about 1055 and 1250 $cm^2 V^{-1} s^{-1}$, respectively.^{18,19} However, a systematic study carried out by Ho et al. highlighted the surface issue of InSe and revealed that the formation of surface oxide in InSe upon exposure to air greatly affects the carrier-transport property.²⁰ They reported a mobility of 423 $cm^2 V^{-1} s^{-1}$ with a dry oxide formed on InSe.²⁰ A key problem with much of the literature on improving the mobility of InSe points out that the trap states at the InSe/substrate interface and the oxidation of InSe in ambient condition greatly affect the carrier-transport properties. A more practical solution for this problem is to upgrade the internal properties of the InSe crystal by doping a ternary element.

For the present work, we have chosen tin (Sn) as the doping element to engineer the $In_{1-x}Sn_xSe$ crystal as Sn atoms behave as a shallow donor in InSe without deteriorating their property.^{21,22} The electrical measurements for $In_{1-x}Sn_xSe$ ultrathin flakes with different concentrations of Sn from 0 to 10% reveal that 1% Sn doping enhances the mobility greatly. We demonstrated the effect of different substrates in the carrier transport of $In_{1-x}Sn_xSe$ phototransistors. A systematic spectral analysis and theoretical calculations were performed to study the underlying mechanisms, which can be realized with the reduction in oxide states and band dispersion of the $In_{1-x}Sn_xSe$ crystals. Furthermore, the gate tunable $In_{1-x}Sn_xSe$ phototransistor featuring high sensitivity and optical gain outperforms all the previously reported InSe devices.^{17,23–25}

EXPERIMENTAL SECTION

InSnSe Single-Crystal Growth. Bridgman technique was used for $In_{1-x}Sn_xSe$ single-crystal growth similar to the 1% Sn-doped InSe crystals previously reported.²¹ The molar mixture of 99.999% pure Sn (1, 5, 10%), In, and Se compounds purchased from Sigma-Aldrich was

placed in evacuated (10^{-4} Pa) conical quartz ampoules. It was heated to 600 °C for 48 h in a horizontal furnace for the synthesis of single crystals following batch homogenization. Before pulling, heat-treatment was carried out for the ampoules and the melt at 850 °C for 24 h. When the ampoule tip was filled with the melt, the ampoule was lowered through a temperature gradient of 1 °C at a rate of 0.1 $mm h^{-1}$. The as-grown $In_{1-x}Sn_xSe$ single crystal with different Sn concentrations was 3 cm long and 1.2 cm in diameter.

Device Fabrication. The $In_{1-x}Sn_xSe$ flakes were prepared by mechanical exfoliation technique using Scotch tape. Polydimethylsiloxane (PDMS) was used for a clean transfer of the exfoliated flakes on the desired substrate. Optical microscopy (Olympus, BX 51M) furnished with a Leica, DFC495 charge-coupled device (CCD) was used to examine the flakes. Atomic force microscopy (AFM) was used to determine the thickness of the flakes. A transmission electron microscopy copper grid was used as a shadow mask and fixed exactly on the flakes using a custom-designed micromanipulator for electrode deposition. The Cr/Au electrodes with a thickness of 7/70 nm were deposited using a thermal evaporator. The poly(methyl methacrylate) (PMMA) encapsulation was carried out by spin-coating PMMA A2 on the flakes at 4500 rpm and baking at 150 °C for 20 min. In order to perform surface modification with octadecyltrichlorosilane (OTS), the SiO_2/Si substrate was cleaned with acetone and isopropanol and dried with pure N_2 gas prior to oxygen plasma treatment. After exposing the SiO_2/Si wafer to oxygen plasma for 10 min (50 W), the wafer is immersed in the OTS/toluene solution and allowed to soak for 1 day. The wafer is rinsed with pure toluene at least five times and ultrasonicated in toluene for 20 min to obtain a cleaner surface.

Characterization Details. An X-ray diffractometer (X'Pert PRO-PANalytical) with Cu $K\alpha$ radiation was employed to record the X-ray diffraction (XRD) pattern of InSnSe flakes in the 2θ range from 10° to 80° at room temperature. The electrical measurements were recorded using a Keithley 2400 electrometer and an Agilent 4156C semiconductor parameter analyzer. A 633 nm wavelength He-Ne laser was used for photoresponse measurements. A Jodson spectrometer equipped with a Horiba Sincerity detector was used to record the photoluminescence (PL) spectrum (excitation energy, $E_{exc} = 2.33$ eV). Ultrafast optical pump-probe measurements were conducted by using a home-built setup. The detailed configuration can be found elsewhere.²⁶ The photon energy and power of the pump

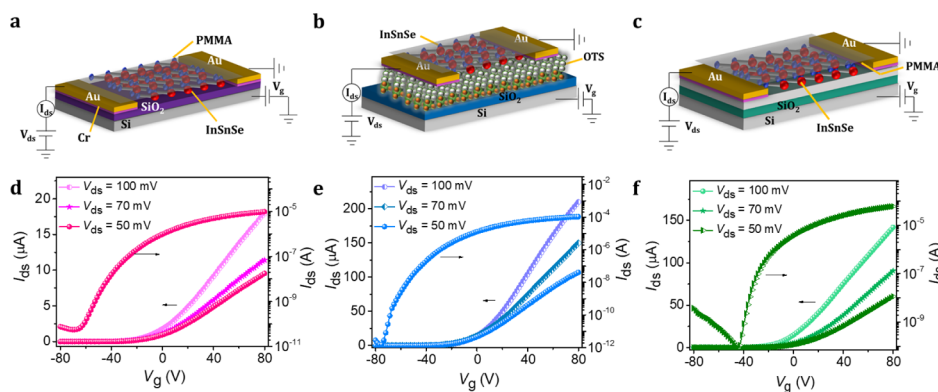


Figure 2. Transfer characteristics of the field-effect transistor on different substrates. (a–c) are the schematic depiction of the PMMA-encapsulated InSnSe FET on SiO₂/Si, OTS-modified SiO₂/Si and PMMA/SiO₂/Si substrate, respectively. (d–f) are the I_{ds} – V_g characteristic curves of the device measured at different V_{ds} in the dark condition on SiO₂/Si, OTS-modified SiO₂/Si and PMMA/SiO₂/Si substrate, respectively.

were ~ 1.57 eV and ~ 12 mW. The photon energy and power of the probe were ~ 1.60 eV and ~ 4 mW. The spot sizes were ~ 700 nm. A Jodson micro-Raman spectrometer equipped with an Olympus CX41 optical microscope and Jobin Won Horiba S Drive-500 Sincerity detector ($E_{exc} = 2.33$ eV, grating = 1800 g mm⁻¹) were used to record the Raman spectra of the In_{1-x}Sn_xSe flakes. The spectrometer was calibrated to the Si peak at 520 cm⁻¹ prior to the spectral acquisition. X-ray photoelectron spectroscopy (XPS) spectra were measured using ESCALAB 250, VG Scientific, coupled with a monochromatic X-ray source (1486.6 eV Al K α). The XPS spectra were calibrated against the binding energy of the adventitious hydrocarbon C 1s signal at 284.8 eV prior to spectral processing. The XPS spectra were processed using CASA XPS software (v.2.3.17, Casa Software Ltd., Wilmslow, Cheshire, U.K.), in which the spectral background subtraction was made by the Shirley-Sherwood method. The quantitative elemental composition was calculated by integrating the intensity of the In 3d_{5/2}, Sn 3d_{5/2}, and Se 3d_{5/2} peaks by taking their respective atomic sensitive factors into account. The atomic sensitivity factors used were 4.359 for In 3d_{5/2}, 4.725 for Sn 3d_{5/2}, and 0.427 for Se 3d_{5/2}.

Theoretical Method. To understand the dramatic mobility enhancement in the 1% Sn-doped InSe, first-principles density functional calculations are performed using the accurate projector augmented wave method as implemented in the Vienna Ab initio Simulation Package.^{27,28} The generalized gradient approximation (GGA)²⁹ is used for the exchange–correlation potential. A large plane-wave energy cut-off of 400 eV is used in all the calculations. For the Brillouin zone (BZ) integrations, a k -point mesh of $10 \times 10 \times 10$ is used. The Sn-doped γ -In_{1-x}Sn_xSe is modeled using virtual crystal approximation, that is, in the self-consistent electronic structure calculations, and the number of conduction electrons is increased by 0.01 and 0.02 per formula unit, respectively, for the 1 and 2% Sn-doped InSe.

RESULTS AND DISCUSSION

The In_{1-x}Sn_xSe crystals with different concentrations of Sn ($x = 0, 1, 5,$ and 10%) were grown by Bridgman technique as detailed in the **Experimental Section**. The layered crystal structure of γ -In_{1-x}Sn_xSe with a hexagonal lattice is shown in **Figure 1a**. The XRD pattern with their respective strong diffraction peaks (**Figure 1b**) confirms the rhombohedral phase of the γ -In_{1-x}Sn_xSe preferred oriented crystal.²¹ According to the standard data file (JCPDS PDF 71-0447) of InSe, the lattice constants were determined to be $a = b = 0.4$ nm and $c = 2.49$ nm. A few layers of In_{1-x}Sn_xSe crystals ($x = 0, 1, 5,$ and 10%) were obtained by mechanical exfoliation and transferred on the SiO₂/Si substrate using PDMS. The uniform distribution of In, Sn, and Se elements in the InSnSe was

confirmed by field emission scanning electron microscopy equipped with energy-dispersive X-ray spectroscopy as shown in **Figure S1**. The electron probe micro-analysis was used to verify the atomic ratio of In, Sn, and Se elements in the as-grown In_{1-x}Sn_xSe crystals as in **Table S1**. The In_{1-x}Sn_xSe flakes with a thickness of ~ 20 nm were chosen for device fabrication using AFM as shown in **Figure S2**. The Cr/Au electrodes (7/70 nm) with a channel length of $12 \mu\text{m}$ was deposited on the flakes using thermal evaporation technique. The transfer curve measured for the few-layered In_{1-x}Sn_xSe flakes with different Sn concentrations in a back-gated field effect transistor configuration (inset of **Figure 1c**) at $V_{ds} = 0.1$ V is depicted in **Figure 1c**. The field effect mobility, μ_e was determined from the transfer curve using the equation¹⁷

$$\mu_e = \frac{L}{WCV_{ds}} \left(\frac{dI_{ds}}{dV_g} \right) \quad (1)$$

where L is the channel length, W is the channel width, C is the capacitance per unit area of the dielectrics ($C = \epsilon_0 \epsilon_r / d$, ϵ_0 —permittivity of free space, ϵ_r —relative permittivity of the dielectric and d —thickness of the dielectric). **Figure 1d** representing the calculated mobility μ_e as a function of Sn concentration indicates that mobility enhances for 1% of Sn doping but decreases for 5 and 10%. The same trend in mobility is observed for the ultrathin In_{1-x}Sn_xSe flakes ($x = 0, 1, 5,$ and 10%) as shown in **Figure S3**. The In_{1-x}Sn_xSe ($x = 1\%$, hereafter mentioned as InSnSe) crystal which exhibits nearly 10 times enhancement in mobility when compared to InSe without doping (at the same conditions) is chosen for further studies.

There are three major parameters which affect the performance of InSnSe-based devices such as (i) surface oxidation, (ii) substrate effect, and (iii) thickness of the flakes.^{18–20,30} The pure InSe readily adsorbs the atmospheric moisture and forms stable oxides affecting the carrier transport in the material.^{20,31} Thus, the mobility of electrons might decrease, resulting in the low performance of the device. In order to prevent surface oxidation, a thin layer of (PMMA) is spin-coated on the device encapsulating the InSnSe flakes (**Figure 2a–c**). The oxide dielectric like SiO₂ has hydroxyl groups naturally formed on the surface with oxygen and water in the atmosphere.^{18,32} These hydroxyl groups act as charged impurities and carrier scattering centers, increasing the surface roughness.^{18,19,33,34} Ultimately, the carrier mobility is greatly

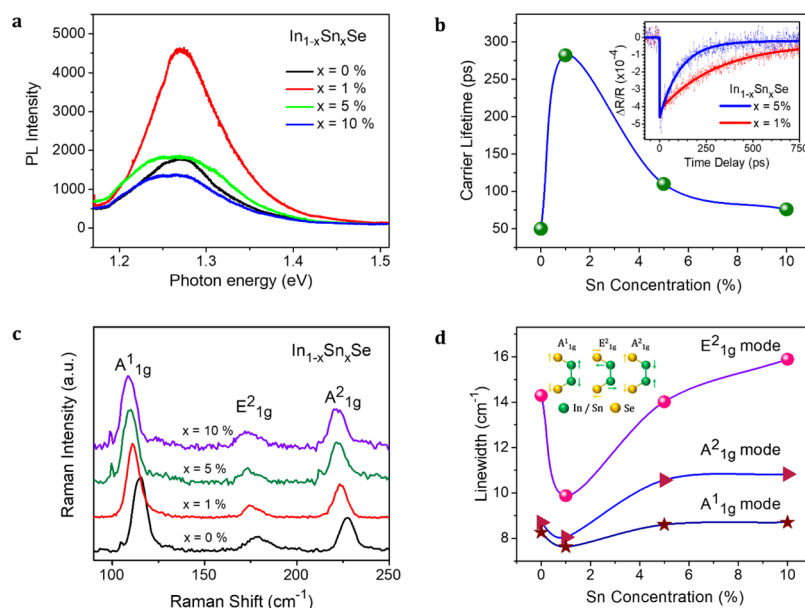


Figure 3. PL, transient reflectivity measurements, and Raman spectra of the exfoliated $\text{In}_{1-x}\text{Sn}_x\text{Se}$ crystal. (a) PL spectra for different Sn concentrations in the $\text{In}_{1-x}\text{Sn}_x\text{Se}$ crystal. (b) Relaxation times of transient reflectivity as a function of Sn concentration. The inset shows the representative transient reflectivity measurements for 1% (in red dots) and 5% Sn (in blue dots). The fitting curves are shown by solid lines. (c) Raman spectra of the $\text{In}_{1-x}\text{Sn}_x\text{Se}$ crystal with different Sn contents. (d) FWHM of the Raman modes as a function of Sn concentration. The inset depicts the schematic of the different vibrational modes in the InSnSe crystal.

reduced because of the trap states in the interface between the substrate and the material. Hence, we measure the InSnSe flakes on surface-modified SiO_2 using a self-assembled OTS monolayer and PMMA coating as depicted in Figure 2b,c, respectively. As the ultrathin flakes suffer extensive carrier scattering because of the close interaction of the carriers with the trap states,³⁰ the thickness of the InSnSe flakes was chosen to be ~ 20 nm. The $I_{\text{ds}}-V_{\text{g}}$ characteristic curves of the device measured from -80 to 80 V at different V_{ds} on SiO_2/Si , OTS/ SiO_2/Si , and PMMA/ SiO_2/Si substrate with flakes encapsulated with PMMA is presented in Figure 2d–f, respectively. The mobility estimated using eq 1 for a number of InSnSe devices on the SiO_2/Si substrate with increased flake thickness and PMMA encapsulation is 281 ± 24 $\text{cm}^2 \text{V}^{-1} \text{s}^{-1}$. This value is further enhanced for the InSnSe devices on OTS/ SiO_2/Si and PMMA/ SiO_2/Si encapsulated with PMMA as 1303 ± 67 and 2560 ± 240 $\text{cm}^2 \text{V}^{-1} \text{s}^{-1}$, respectively. The parameters length, width, and the slope used in estimating the mobility are clearly defined in Figure S4 and Table S2. The mobility enhancement is almost twice on the PMMA substrate when compared to pure InSe previously reported^{18,19} at the same conditions (Table S3). The n-type transport behavior of InSnSe crystals was observed on all the three dielectrics used, including the h-BN-encapsulated device as shown in Figure S5. The reason for such an improvement in mobility for 1% Sn-doped samples when compared to pure InSe, 5 and 10% Sn doping can be explained on the basis of crystal quality as follows.

The PL spectra of $\text{In}_{1-x}\text{Sn}_x\text{Se}$ flakes with different Sn concentrations (x) are shown in Figure 3a. The PL peak intensity of 1% Sn doping increases almost three times compared with the other samples (Figure S6a). Ultrafast optical pump-probe measurements were conducted to study the carrier lifetimes. The representative transient reflectivity curves for 1 and 5% Sn doping are shown in the inset of Figure 3b. The relaxation time of 1% Sn-doped InSnSe is longer than

that of the 5% one. This reveals the longer carrier lifetime in the $\text{In}_{1-x}\text{Sn}_x\text{Se}$ crystal with 1% Sn doping as the reflectivity changes of the optical probe could indicate the carrier density.³⁵ All experimental traces were fitted with an exponential decay function and a constant function to obtain the time constants of exponential relaxation. The average carrier lifetimes of each sample with different Sn concentrations are summarized in Figure 3b. The longer carrier lifetime of 1% Sn doping results in a stronger PL intensity as shown in Figure 3a. The full width at half-maximum (FWHM) of the PL peaks as a function of Sn content represented in the inset of Figure S6a marks the narrowing of the PL peak for $x = 1\%$ and broadening for $x = 5, 10\%$. The broadening of the PL peak with 5 and 10% Sn doping can be attributed to the formation of defect states in the $\text{In}_{1-x}\text{Sn}_x\text{Se}$ with Sn doping.³⁶ However, the narrowing of the PL peak and increase in intensity signifies the reduction of defects and longer carrier lifetime in the $\text{In}_{1-x}\text{Sn}_x\text{Se}$ crystal with 1% Sn doping. To affirm the interpretation, the Raman spectrum was recorded for $\text{In}_{1-x}\text{Sn}_x\text{Se}$ ($x = 0, 1, 5$ and 10%) samples with wavenumber range from 90 to 250 cm^{-1} (Figure 3c). The prominent Raman peaks centered at $115.4, 178.9,$ and 227.5 cm^{-1} correspond to the $A_{1g}^1, E_{1g}^2,$ and A_{1g}^2 phonon modes confirming the γ - $\text{In}_{1-x}\text{Sn}_x\text{Se}$ polytype.³⁷ A substantial red shift is observed in the A_{1g}^1 mode because of Sn doping in $\text{In}_{1-x}\text{Sn}_x\text{Se}$ (Figure S6b). The FWHM of the observed phonon modes plotted as a function of Sn doping shown in Figure 3d evidently signifies the narrowing of peaks for 1% Sn doping which broadens for 5 and 10%. However, the E_{1g}^2 mode shows a significant change in the FWHM when compared to other modes because of the bond stretching involved in the vibration pattern as illustrated in the inset of Figure 3d. Thus, the FWHM of PL and Raman peaks with respect to Sn doping validates that there is a reduction of defect states in 1% Sn-doped InSnSe crystals. As the $\text{In}_{1-x}\text{Sn}_x\text{Se}$ crystal is an n-type semiconductor as observed from the transfer curves (Figures 1c and 2d–f), there is a

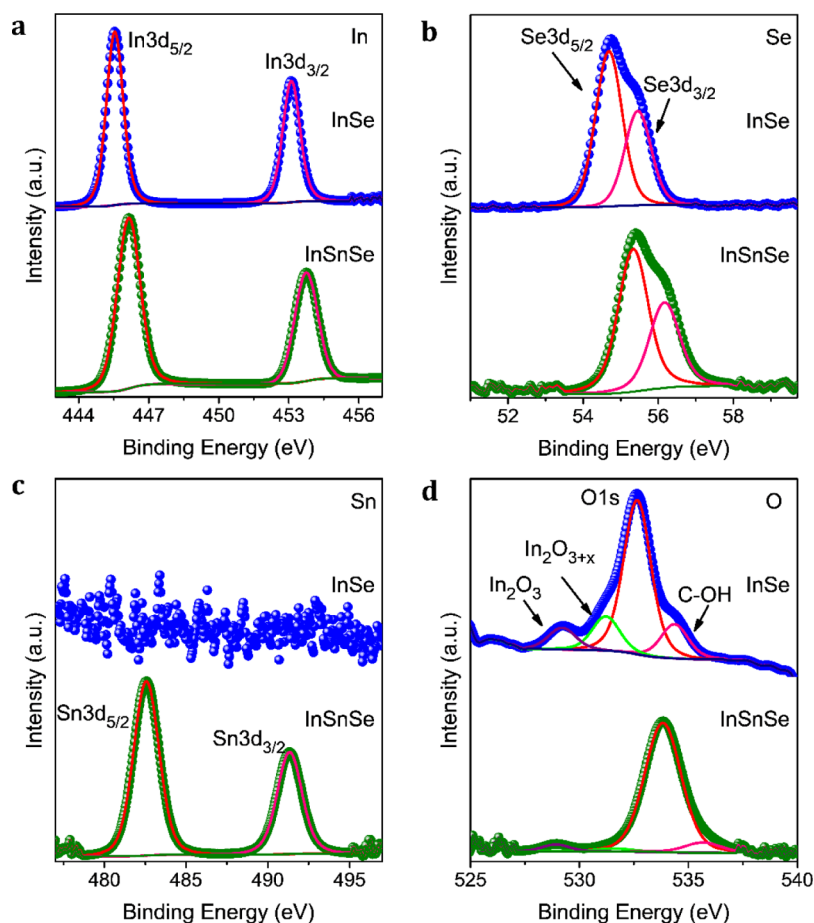


Figure 4. XPS spectra of InSe (top) and InSnSe (bottom) crystals show the doublets caused by the 3d spin–orbit couplings in (a) In (b) Se and (c) Sn. (d) The deconvoluted spectral components of the O 1s peak show the oxidation behavior of InSe and InSnSe crystals.

possibility of more In atoms in the crystal at interstitial sites acting as the electron source. In such a case, the most stable defect in the crystal is an Se vacancy because of the low enthalpy of vaporization for Se atoms.^{38,39} These Se vacancies are the home for the chemisorbed oxygen atoms as the process is energetically favored and forms an In–O–Se bond. This disturbance in the lattice causes weakening of the neighboring In–Se bond and more chemisorbed oxygen atoms replace Se atoms, resulting in the formation of a stable In_2O_3 phase. The localized distortion in the crystal lattice leads to a further oxidation process as reported by Shi et al.³⁸ This In_2O_3 formed acts as a hole doping to the crystal, degrading the carrier transport and obvious mobility of the electrons.^{20,39} However, in our study because of Sn substitutional doping for In, the formation of In_2O_3 may be reduced as the phase equilibrium is disturbed.^{30,40}

To validate the above interpretation, XPS studies were carried out for InSe and InSnSe crystals as shown in Figure 4. The XPS analysis revealed the constituent elements in InSe and InSnSe crystals along with an insight into their oxidation states. The Indium 3d_{5/2} and 3d_{3/2} doublets were observed at 445.6 and 453.2 eV in pure InSe, whereas a 0.4 eV low binding energy location was observed for InSnSe at 445.2 and 452.8 eV, respectively (Figure 4a). Similarly, Se doublets 3d_{5/2} and 3d_{3/2} were identified at 55.4 and 56.2 eV for InSe and with a 0.7 eV lower binding energy for InSnSe at 54.7 and 55.7 eV (Figure 4b). The doublets at 482.6 and 491.3 eV showed the presence of Sn3d_{5/2} and Sn3d_{3/2} peaks in InSnSe, which are

absent in the InSe crystal (Figure 4c). The red shift in the component peaks of InSnSe can be attributed to the binding energy shift as a result of the incorporation of Sn in the InSe crystal structure. Figure 4d shows the comparative O 1s peak of InSe and InSnSe samples, where both the spectra showed an asymmetric peak line shape, which was deconvoluted into four Lorentzian components (Figure 4d). In the case of InSe, the components in the lower energy tail at 529.2 and 531.4 eV were attributed to the In_2O_3 ^{41,42} and $\text{In}_2\text{O}_{3+x}$ ^{20,41} peaks along with the central maximum at 532.6 eV and higher energy tail peaking at 534.4 eV correspond to the C–O and hydroxide bonds, respectively. Comparatively, InSnSe possessed all these component peaks with a red shift of 0.3 eV but with much-reduced intensities. Moreover, the Lorentzian line shape fitting of the components showed that the InSe has a 12.5% concentration of $\text{In}_2\text{O}_{3+x}$ whereas the Sn-doped InSe accounted for a lower value of 2.3%, strongly supporting the suppressed oxide formation in InSnSe samples. Hence, the decreased defect states leading to increased carrier lifetime is one of the possible reasons for the increased mobility in 1% Sn doping in $\text{In}_{1-x}\text{Sn}_x\text{Se}$, and the increase in Sn doping (5 and 10%) can have more Sn interstitials, which behave as scattering centers affecting the reduced mobility.

To uncover the microscopic mechanism of the dramatic mobility enhancement in the 1% Sn-doped InSe, first-principles density functional calculations for pure, 1 and 2% Sn-doped InSe are carried out (see the Theoretical Method and Supporting Information Note 4 for details), and the

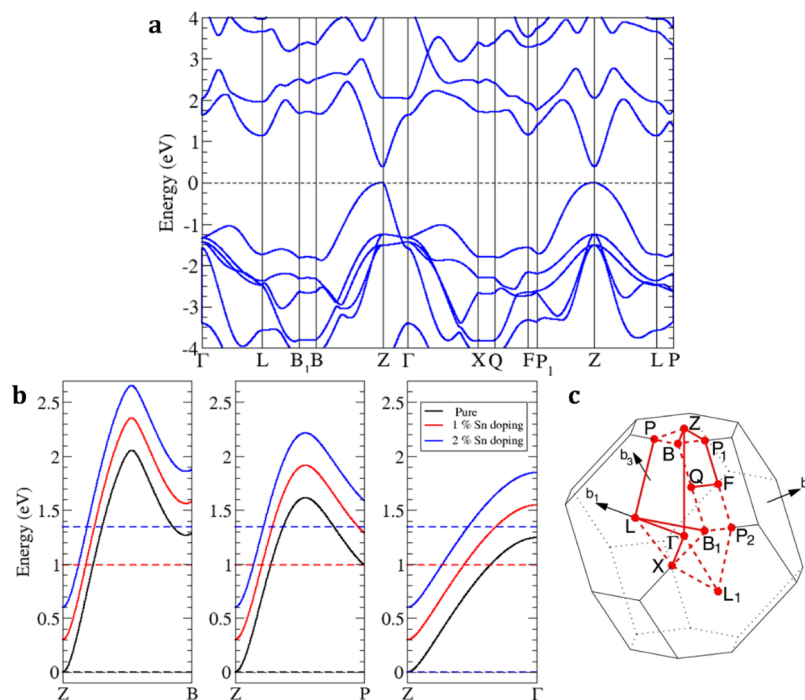


Figure 5. (a) The GGA band structure of pure InSe and (b) the lowest conduction band near the Z-point along three high symmetry lines in (c) the BZ for pure, 1 and 2% Sn-doped InSe. In (b), the dashed red and blue horizontal lines denote the Fermi levels for the 1 and 2% Sn-doped InSe, respectively. Note that in (a), zero refers to the top of the valence band and in (b) zero is set to the bottom of the conduction band for pure InSe.

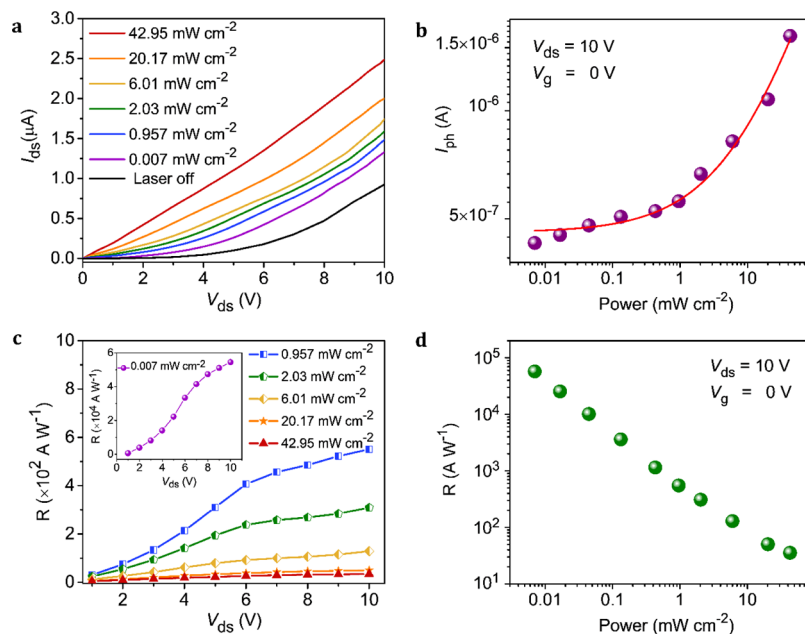


Figure 6. Photoresponse of the few-layered InSnSe phototransistor. (a) I_{ds} – V_{ds} curves of the InSnSe phototransistor at $V_g = 0$ V with a laser excitation of 633 nm wavelength at different power densities. (b) Photocurrent as a function of incident laser power density at $V_{ds} = 10$ V and $V_g = 0$ V. (c) Responsivity (R) as a function of applied drain–source voltage at different laser power densities with $V_g = 0$ V. The inset represents the R vs V_{ds} plot at a laser power density of 0.007 mW cm^{-2} . (d) Responsivity as a function of incident laser power density at $V_{ds} = 10$ V and $V_g = 0$ V.

calculated band structures are plotted in Figure 5. Pure InSe is found to be a direct band gap semiconductor with the electron pocket at the Z-point in the BZ (Figure 5). The shape of this electron pocket is unaffected by the Sn doping, and consequently, the calculated effective masses for all three systems are identical (see Table S4). Within the semiclassical Boltzmann transport theory, the conductivity for an electron-doped semiconductor can be written⁴³ as $\sigma = ne\mu = ne^2\tau/m^*$

and $\mu = e\tau/m^*$, where τ and n are, respectively, the electron lifetime and concentration, that is, $\sigma/\tau \propto n$ and $\mu \propto \tau$ if the effective mass m^* is constant. Using the GGA band structure (Figure 5), we calculate σ/τ as a function of n (see Supporting Information Note 4). Indeed, we find that $\sigma/\tau \propto n$ (see Figure S9). Therefore, we can conclude that the enhanced electron mobility in the 1% Sn-doped InSe samples is caused by an increase in the carrier lifetime because of the improved crystal

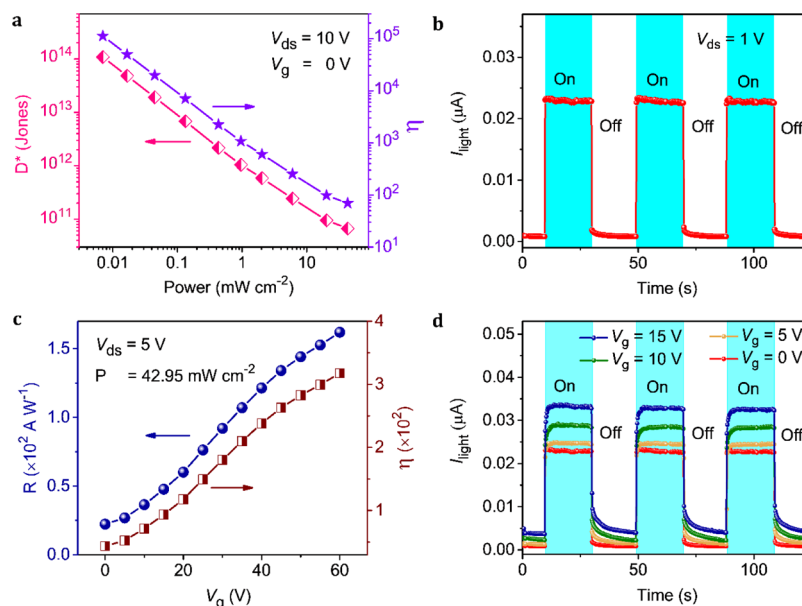


Figure 7. Performance of the few-layered InSnSe phototransistor. (a) Detectivity (D^*) and photogain (η) as a function of laser power density at $V_{ds} = 10$ V and $V_g = 0$ V. (b) Photo-switching characteristics of the device at $V_{ds} = 1$ V and laser power density of 0.431 mW cm^{-2} . (c) Responsivity (R) and Photogain (η) as a function of applied gate voltage (V_g) at $V_{ds} = 5$ V and $P = 42.95$ mW cm^{-2} . (d) Photo-switching stability of the device at different V_g with $V_{ds} = 1$ V.

quality and the reduced oxide phase compared to undoped InSe.

On the basis of the above study, few-layered InSnSe devices fabricated on the SiO_2/Si substrate with PMMA encapsulation have been employed as a high-performance phototransistor. The thickness of the flake chosen for phototransistor measurement is ~ 13 nm as determined with AFM as shown in Figure S10a. The optical microscopy image of the InSnSe device is depicted in Figure S10b. The effective area of the phototransistor is ~ 115 μm^2 . The linear change in drain-source current (I_{ds}) for the applied bias at a different gate voltage (V_g) from 0 to 80 V (Figure S11a) assures a good ohmic contact amidst the InSnSe flakes and Au electrodes. The transfer curve measured by sweeping V_g from -60 to 60 V at $V_{ds} = 5$ V under dark and laser illumination ($\lambda = 633$ nm) in the back-gate transistor configuration is represented in Figure S11b. It indicates a high on/off ratio as $\sim 10^8$ (Figure S11c) and the increased drain-source current under laser illuminated condition manifests the potential of InSnSe flakes as a phototransistor.⁶ To explore the photodetecting properties of InSnSe device in detail, we measured the drain-source current for the applied voltage bias under different power intensities of 633 nm laser without the application of gate voltage as shown in Figure 6a. The I_{ds} - V_{ds} curve increases with an increase in laser power intensity and stays marginally nonlinear without saturation at a higher voltage bias (Figure 6a). The photocurrent ($I_{ph} = I_{light} - I_{dark}$) generated plotted as a function different laser power intensity is presented in Figure 6b. Fitting to the power law, $I_{ph} \propto P^\alpha$, the value of α obtained is 0.62, which is less than 1, signifying that photocarrier generation and recombination involve trap states in the device.⁴⁴ However, at a higher laser power intensity >1 mW cm^{-2} , the power law fitting yields α , which is larger than 1, emphasizing the superlinear power dependence of the photocurrent (Figure S12). This superlinear behavior of the photocurrent can be due to the quasi-Fermi levels shifting at higher laser power with an increase in photocarriers. As the

quasi-Fermi levels shift to the conduction and valence band states, the recombination rate becomes slower, which results in an enhanced carrier lifetime and shows a superlinear photoresponse.^{45,46} The photoresponsivity (R) of the InSnSe devices was calculated using the following equation

$$R = \frac{I_{ph}}{P \times S} = \frac{I_{light} - I_{dark}}{P \times S} \quad (2)$$

where P is the laser power intensity and S is the illuminated area of the device. Figure 6c shows the responsivity of the device as a function of the applied drain-source voltage for different laser powers and the inset represents the R - V_{ds} plot for a laser power of 7.021 $\mu\text{W cm}^{-2}$. The photoresponsivity increases with increase in applied voltage bias, which can be attributed to the reduction in carrier transit time (τ_t) with enhanced drift velocity according to the relation, $V_{ds} = L^2/\mu\tau_t$ where μ is the carrier mobility.⁶ The photoresponsivity of the device as a function of laser power at constant V_{ds} is plotted in Figure 6d. The responsivity increases with a decrease in laser power, asserting that the high photosensitivity of the detector and the maximum photoresponsivity of the device without gate voltage at $V_{ds} = 10$ V ($P = 7.021$ $\mu\text{W cm}^{-2}$) is 5.7×10^4 A W^{-1} .

Another parameter which signifies the device sensitivity is detectivity (D^*), which is inversely related to noise equivalent power (NEP) according to the equation⁴⁷

$$D^* = \frac{(S\Delta f)^{1/2}}{\text{NEP}} \quad (3)$$

where S is the active area of the device and Δf is the measuring bandwidth and is inversely related to the response time. NEP is the minimum optical illumination that a photodetector can distinguish from noise and is proportional to the root mean square noise current, $\text{NEP} = I_n/R$. Noise current (I_n) is related to the dark current (I_{dark}) as $I_n^2 = 2eI_{dark}\Delta f$ where e is the electronic charge.⁴⁷ D^* plotted as a function of illuminated laser power as shown in Figure 7a specifies the maximum

detectivity of the device to be 1×10^{14} Jones at $V_{ds} = 10$ V and $P = 7.021 \mu\text{W cm}^{-2}$. The parameters used in calculating D^* have been elaborated in Supporting Information Note 6. In the metal–semiconductor–metal device, surface band bending occurs in the metal–semiconductor junction because of the difference in the Fermi level energy and work function between the semiconductor and metal. When the semiconductor is illuminated with energy above the band gap, the generated photocarriers are spatially separated with the potential barriers caused by the surface band bending, giving a large photoconductive gain.⁴⁸ In addition, the longer carrier lifetime (τ) of the InSnSe crystal caused by Sn doping aids in increasing the photoconductive gain,⁴ which results in the high photoresponsivity (R),⁴⁹ and in turn reduces the NEP. Consequently, the high detectivity was obtained in the device at 633 nm. The highest detectivity estimated for the InSnSe device when compared to the previous reports of InSe photodetectors^{17,23,24,50} and vertical heterostructures^{51–53} manifests the better photodetecting performance of the InSnSe devices with low NEP.

Photogain (η) defined as the number of electrons detected per incident photon can be estimated using the equation

$$\eta = \frac{Rhc}{e\lambda} \quad (4)$$

where R is the photoresponsivity, h is Planck's constant, c is the speed of light, e is the electronic charge, and λ is the wavelength of the incident light.²¹ Figure 7a illustrates the photogain of the InSnSe device as a function of laser power at $V_{ds} = 10$ V and the maximum photogain obtained is 1.1×10^5 , which is high compared to previously reported InSe-based photodetectors.¹⁷ The enhanced photogain of the InSnSe device (Figure S13) shows higher optical absorption of the InSnSe flakes with fewer trap states and reduced recombination rate.⁵ The time-resolved photoresponse of the InSnSe device under pulsed illumination of 633 nm laser ($V_{ds} = 1$ V, $P = 0.431 \text{ mW cm}^{-2}$) shown in Figure 7b demonstrates the photoswitching characteristics of the device. It indicates the stable current flow in the photodetector at both on/off laser illumination. Figure S14 shows the photoexcitation and de-excitation of carriers at laser on and off states, respectively. The photoresponse time and recovery time of the device are estimated to be 25 and 10 ms, respectively. The InSnSe phototransistor also responds to infrared laser illumination as shown in Figure S15.

The responsivity and photogain of the InSnSe device (633 nm laser) with the application of back-gate voltage at constantly applied bias were estimated using eqs 2 and 4, respectively, as shown in Figure 7c. A back-gate voltage of 60 V enhanced the value of R and η by seven times at $V_{ds} = 5$ V and $P = 42.95 \text{ mW cm}^{-2}$ (Figure 7c). The stable photoswitching characteristics of the InSnSe device at different back-gate voltages are shown in Figure 7d. It again validates the increase in photocurrent of the device with back-gating. The maximum photoresponsivity obtained for the InSnSe device at $V_g = 40$ V and $V_{ds} = 5$ V with a laser power of $7.021 \mu\text{W cm}^{-2}$ is $3 \times 10^5 \text{ A W}^{-1}$ (Table S5), which is comparable to the other 2D material-based phototransistors.^{54–56} When the gate voltage is not applied or it is less than the threshold voltage of the phototransistor, there can be a Schottky barrier formed between the Au electrode and InSnSe because of the difference in their Fermi levels. When the gate voltage is greater than the threshold voltage, thermionic current along with the tunneling

and photocurrent reduces the barrier height by reducing the depletion region between Au and InSnSe. Therefore, more photocurrent is extracted effectively, leading to the enhanced photoresponsivity of the InSnSe device.^{17,23}

CONCLUSIONS

In conclusion, we have presented a detailed study on enhancing the intrinsic mobility of $\text{In}_{1-x}\text{Sn}_x\text{Se}$ -layered flakes with atomic doping. The electrical transport study of $\text{In}_{1-x}\text{Sn}_x\text{Se}$ ($x = 0, 1, 5$ and 10%) ultrathin flakes on an SiO_2/Si substrate suggests that 1% Sn-doped $\text{In}_{1-x}\text{Sn}_x\text{Se}$ (InSnSe) flakes exhibit higher mobility intrinsically. Further electrical measurements of InSnSe devices with PMMA encapsulation and surface modified substrates (OTS, PMMA) show enhancement in mobility up to $2560 \pm 240 \text{ cm}^2 \text{ V}^{-1} \text{ s}^{-1}$. The PL and Raman spectral studies of $\text{In}_{1-x}\text{Sn}_x\text{Se}$ ($x = 0, 1, 5$, and 10%) emphasize the narrowing of the peak for 1% Sn-doped flakes, indicating the reduction in intrinsic defects in the crystal. XPS spectra of $\text{In}_{1-x}\text{Sn}_x\text{Se}$ ($x = 0$ and 1%) crystals confirm the oxide reduction in 1% Sn-doped flakes. Moreover, the theoretical calculation reveals that the electron effective mass m^* is unaffected by the Sn-doping. Taken together with the transient reflectivity measurements, the results suggest that the longer carrier lifetime because of a reduction in the oxide phase and also the improved crystal quality of the 1% Sn-doped InSe samples cause the enhanced mobility of InSnSe thin flakes. The simplified device of InSnSe flakes with PMMA encapsulation has been demonstrated as a highly sensitive gate-tunable phototransistor with maximum photoresponsivity and photogain as $3 \times 10^5 \text{ A W}^{-1}$ and 0.5×10^6 , respectively, at $V_g = 40$ V. The detectivity of the InSnSe was estimated to be 1×10^{14} Jones without the gate voltage. Thus, we have devised a methodology of doping engineering InSe to obtain InSnSe phototransistors with intrinsically enhanced mobility and optoelectronic properties.

ASSOCIATED CONTENT

Supporting Information

The Supporting Information is available free of charge on the ACS Publications website at DOI: 10.1021/acsami.9b06433.

Material characterization of InSnSe flakes; InSnSe device performance with different substrates; PL and Raman spectrum analysis; computational details (GGA and HSE); optical microscopy image of the device and gate-dependent photocurrent measurement of the InSnSe phototransistor; analysis of the time-resolved photocurrent measurement; and comparison of the InSnSe device with a previous report (PDF)

AUTHOR INFORMATION

Corresponding Author

*E-mail: yfchen@phys.ntu.edu.tw.

ORCID

Christy Roshini Paul Inbaraj: 0000-0002-8776-9917

Roshan Jesus Mathew: 0000-0002-0913-6321

Rajesh Kumar Ulaganathan: 0000-0001-8886-6332

Raman Sankar: 0000-0003-4702-2517

Hung-I Lin: 0000-0001-9849-3138

Yu-Ming Liao: 0000-0002-8696-7313

Kung-Hsuan Lin: 0000-0003-2731-5400

Yit-Tsong Chen: 0000-0002-6204-8320

Author Contributions

The paper was written through the contributions of all the authors. All the authors have given approval to the final version of the paper.

Notes

The authors declare no competing financial interest.

ACKNOWLEDGMENTS

This work was sponsored by the "Advanced Research Center for Green Materials Science and Technology" from the Featured Area Research Center Program within the framework of the Higher Education Sprout Project by the Ministry of Education (107L9006) and the Ministry of Science and Technology in Taiwan (MOST 107-3017-F-002-001). C.R.P.I. would like to thank the support of the Taiwan Internal Graduate Program (TIGP), Institute of Physics, Academia Sinica, Taipei, Taiwan, and National Tsing Hua University, Hsinchu, Taiwan. C.R.P.I. would like to acknowledge Prof. Mario Hofmann and Prof. Ya-Ping Hsieh for their support and discussions.

REFERENCES

- (1) Bae, S.; Kim, H.; Lee, Y.; Xu, X.; Park, J.-S.; Zheng, Y.; Balakrishnan, J.; Lei, T.; Ri Kim, H.; Song, Y. I.; Kim, Y.-J.; Kim, K. S.; Özyilmaz, B.; Ahn, J.-H.; Hong, B. H.; Iijima, S. Roll-to-Roll Production of 30-Inch Graphene Films for Transparent Electrodes. *Nat. Nanotechnol.* **2010**, *5*, 574–578.
- (2) Wang, Q. H.; Kalantar-Zadeh, K.; Kis, A.; Coleman, J. N.; Strano, M. S. Electronics and Optoelectronics of Two-Dimensional Transition Metal Dichalcogenides. *Nat. Nanotechnol.* **2012**, *7*, 699–712.
- (3) Novoselov, K. S.; Geim, A. K.; Morozov, S. V.; Jiang, D.; Katsnelson, M. I.; Grigorieva, I. V.; Dubonos, S. V.; Firsov, A. A. Two-Dimensional Gas of Massless Dirac Fermions in Graphene. *Nature* **2005**, *438*, 197–200.
- (4) Buscema, M.; Island, J. O.; Groenendijk, D. J.; Blanter, S. I.; Steele, G. A.; Van Der Zant, H. S. J.; Castellanos-Gomez, A. Photocurrent Generation with Two-Dimensional van Der Waals Semiconductors. *Chem. Soc. Rev.* **2015**, *44*, 3691–3718.
- (5) Xie, C.; Mak, C.; Tao, X.; Yan, F. Photodetectors Based on Two-Dimensional Layered Materials Beyond Graphene. *Adv. Funct. Mater.* **2017**, *27*, 1603886.
- (6) Lopez-Sanchez, O.; Lembke, D.; Kayci, M.; Radenovic, A.; Kis, A. Ultrasensitive Photodetectors Based on Monolayer MoS₂. *Nat. Nanotechnol.* **2013**, *8*, 497–501.
- (7) Iqbal, M. W.; Iqbal, M. Z.; Khan, M. F.; Shehzad, M. A.; Seo, Y.; Park, J. H.; Hwang, C.; Eom, J. High-Mobility and Air-Stable Single-Layer WS₂ Field-Effect Transistors Sandwiched between Chemical Vapor Deposition-Grown Hexagonal BN Films. *Sci. Rep.* **2015**, *5*, 10699.
- (8) Nguyen, D. A.; Oh, H. M.; Duong, N. T.; Bang, S.; Yoon, S. J.; Jeong, M. S. Highly Enhanced Photoresponsivity of a Monolayer WSe₂ Photodetector with Nitrogen-Doped Graphene Quantum Dots. *ACS Appl. Mater. Interfaces* **2018**, *10*, 10322–10329.
- (9) Radisavljevic, B.; Radenovic, A.; Brivio, J.; Giacometti, V.; Kis, A. Single-Layer MoS₂ transistors. *Nat. Nanotechnol.* **2011**, *6*, 147–150.
- (10) Kim, S.; Konar, A.; Hwang, W. S.; Lee, J. H.; Lee, J.; Yang, J.; Jung, C.; Kim, H.; Yoo, J. B.; Choi, J. Y.; Jin, Y. W.; Lee, S. Y.; Jena, D.; Choi, W.; Kim, K. High-Mobility and Low-Power Thin-Film Transistors Based on Multilayer MoS₂ crystals. *Nat. Commun.* **2012**, *3*, 1011–1017.
- (11) Zhang, Y.; Ye, J.; Matsushashi, Y.; Iwasa, Y. Ambipolar MoS₂ Thin Flake Transistors. *Nano Lett.* **2012**, *12*, 1136–1140.
- (12) Bao, W.; Cai, X.; Kim, D.; Sridhara, K.; Fuhrer, M. S. High Mobility Ambipolar MoS₂ Field-Effect Transistors: Substrate and Dielectric Effects. *Appl. Phys. Lett.* **2013**, *102*, 042104.
- (13) Kim, J. H.; Kim, T. H.; Lee, H.; Park, Y. R.; Choi, W.; Lee, C. J. Thickness-Dependent Electron Mobility of Single and Few-Layer MoS₂ thin-Film Transistors. *AIP Adv.* **2016**, *6*, 065106.
- (14) Das, S.; Chen, H.-Y.; Penumatcha, A. V.; Appenzeller, J. High Performance Multilayer MoS₂ Transistors with Scandium Contacts. *Nano Lett.* **2013**, *13*, 100–105.
- (15) Li, L.; Yu, Y.; Ye, G. J.; Ge, Q.; Ou, X.; Wu, H.; Feng, D.; Chen, X. H.; Zhang, Y. Black Phosphorus Field-Effect Transistors. *Nat. Nanotechnol.* **2014**, *9*, 372–377.
- (16) Kress-Rogers, E.; Nicholas, R. J.; Portal, J. C.; Chevy, A. Cyclotron Resonance Studies on Bulk and Two-Dimensional Conduction Electrons in InSe. *Solid State Commun.* **1982**, *44*, 379–383.
- (17) Tamalampudi, S. R.; Lu, Y.-Y.; Kumar, U. R.; Sankar, R.; Liao, C.-D.; Moorthy, B. K.; Cheng, C.-H.; Chou, F. C.; Chen, Y.-T. High Performance and Bendable Few-Layered InSe Photodetectors with Broad Spectral Response. *Nano Lett.* **2014**, *14*, 2800–2806.
- (18) Feng, W.; Zheng, W.; Cao, W.; Hu, P. Back Gated Multilayer InSe Transistors with Enhanced Carrier Mobilities via the Suppression of Carrier Scattering from a Dielectric Interface. *Adv. Mater.* **2014**, *26*, 6587–6593.
- (19) Sucharitakul, S.; Goble, N. J.; Kumar, U. R.; Sankar, R.; Bogorad, Z. A.; Chou, F.-C.; Chen, Y.-T.; Gao, X. P. A. Intrinsic Electron Mobility Exceeding 10³cm²/(V s) in Multilayer InSe FETs. *Nano Lett.* **2015**, *15*, 3815–3819.
- (20) Ho, P.-H.; Chang, Y.-R.; Chu, Y.-C.; Li, M.-K.; Tsai, C.-A.; Wang, W.-H.; Ho, C.-H.; Chen, C.-W.; Chiu, P.-W. High-Mobility InSe Transistors: The Role of Surface Oxides. *ACS Nano* **2017**, *11*, 7362–7370.
- (21) Inbaraj, C. R. P.; Mathew, R. J.; Haider, G.; Chen, T.-P.; Ulaganathan, R. K.; Sankar, R.; Bera, K. P.; Liao, Y.-M.; Kataria, M.; Lin, H.-I.; Chou, F. C.; Chen, Y.-T.; Lee, C.-H.; Chen, Y.-F. Ultrahigh Performance Flexible Piezopotential Gated In_{1-x}Sn_xSe Phototransistor. *Nanoscale* **2018**, *10*, 18642–18650.
- (22) Hou, X.; Chen, S.; Du, Z.; Liu, X.; Cui, J. Improvement of the Thermoelectric Performance of InSe-Based Alloys Doped with Sn. *RSC Adv.* **2015**, *5*, 102856–102862.
- (23) Feng, W.; Wu, J.-B.; Li, X.; Zheng, W.; Zhou, X.; Xiao, K.; Cao, W.; Yang, B.; Idrobo, J.-C.; Basile, L.; Tian, W.; Tan, P.; Hu, P. Ultrahigh Photo-Responsivity and Detectivity in Multilayer InSe Nanosheets Phototransistors with Broadband Response. *J. Mater. Chem. C* **2015**, *3*, 7022–7028.
- (24) Lei, S.; Ge, L.; Najmaei, S.; George, A.; Kappera, R.; Lou, J.; Chhowalla, M.; Yamaguchi, H.; Gupta, G.; Vajtai, R.; Mohite, A. D.; Ajayan, P. M. Evolution of the Electronic Band Structure and Efficient Photo-Detection in Atomic Layers of InSe. *ACS Nano* **2014**, *8*, 1263–1272.
- (25) Luo, W.; Cao, Y.; Hu, P.; Cai, K.; Feng, Q.; Yan, F.; Yan, T.; Zhang, X.; Wang, K. Gate Tuning of High-Performance InSe-Based Photodetectors Using Graphene Electrodes. *Adv. Opt. Mater.* **2015**, *3*, 1418–1423.
- (26) Lin, K.-H.; Cheng, H.-Y.; Yang, C.-Y.; Li, H.-W.; Chang, C.-W.; Chu, S.-W. Phonon dynamics of single nanoparticles studied using confocal pump-probe backscattering. *Appl. Phys. Lett.* **2018**, *113*, 171906.
- (27) Kresse, G.; Furthmüller, J. Efficient Iterative Schemes for Ab Initio Total-Energy Calculations Using a Plane-Wave Basis Set. *Phys. Rev. B: Condens. Matter Mater. Phys.* **1996**, *54*, 11169–11186.
- (28) Kresse, G.; Furthmüller, J. Efficiency of Ab-Initio Total Energy Calculations for Metals and Semiconductors Using a Plane-Wave Basis Set. *Comput. Mater. Sci.* **1996**, *6*, 15–50.
- (29) Perdew, J. P.; Burke, K.; Ernzerhof, M. Generalized Gradient Approximation Made Simple. *Phys. Rev. Lett.* **1996**, *77*, 3865–3868.
- (30) Liang, G.; Wang, Y.; Han, L.; Yang, Z. X.; Xin, Q.; Kudrynskiy, Z. R.; Kovalyuk, Z. D.; Patane, A.; Song, A. Improved Performance of InSe Field-Effect Transistors by Channel Encapsulation. *Semicond. Sci. Technol.* **2018**, *33*, 06LT01.

- (31) Balitskii, O. A.; Berchenko, N. N.; Savchyn, V. P.; Stakhira, J. M. Characteristics of Phase Formation during Indium Selenides Oxidation. *Mater. Chem. Phys.* **2000**, *65*, 130–135.
- (32) Wang, X.; Xu, J.-B.; Wang, C.; Du, J.; Xie, W. High-Performance Graphene Devices on SiO₂/Si Substrate Modified by Highly Ordered Self-Assembled Monolayers. *Adv. Mater.* **2011**, *23*, 2464–2468.
- (33) Guo, Y.; Wei, X.; Shu, J.; Liu, B.; Yin, J.; Guan, C.; Han, Y.; Gao, S.; Chen, Q. Charge Trapping at the MoS₂-SiO₂ interface and Its Effects on the Characteristics of MoS₂ metal-Oxide-Semiconductor Field Effect Transistors. *Appl. Phys. Lett.* **2015**, *106*, 103109.
- (34) Chan, M. Y.; Komatsu, K.; Li, S.-L.; Xu, Y.; Darmawan, P.; Kuramochi, H.; Nakaharai, S.; Aparecido-Ferreira, A.; Watanabe, K.; Taniguchi, T.; Tsukagoshi, K. Suppression of Thermally Activated Carrier Transport in Atomically Thin MoS₂ on Crystalline Hexagonal Boron Nitride Substrates. *Nanoscale* **2013**, *5*, 9572–9576.
- (35) Yang, C.-Y.; Chia, C.-T.; Chen, H.-Y.; Gwo, S.; Lin, K.-H. Ultrafast carrier dynamics in GaN nanorods. *Appl. Phys. Lett.* **2014**, *105*, 212105.
- (36) Ping, C.; Yue, B.; Zhi, Q. Structural and Photoluminescence Properties of Mn-Doped ZnO Nanocolumns Grown by Cathodic Electrodeposition. *Rare Met. Mater. Eng.* **2016**, *45*, 326–328.
- (37) IKari, T.; Shigetomi, S.; Hashimoto, K. Crystal Structure and Raman Spectra of InSe. *Phys. Status Solidi B* **1982**, *111*, 477–481.
- (38) Shi, L.; Zhou, Q.; Zhao, Y.; Ouyang, Y.; Ling, C.; Li, Q.; Wang, J. Oxidation Mechanism and Protection Strategy of Ultrathin Indium Selenide: Insight from Theory. *J. Phys. Chem. Lett.* **2017**, *8*, 4368–4373.
- (39) Xiao, K. J.; Carvalho, A.; Castro Neto, A. H. Defects and Oxidation Resilience in InSe. *Phys. Rev. B* **2017**, *96*, 054112.
- (40) Jeon, A.-J.; Kim, S.-J.; Lee, S.-H.; Kang, C.-Y. Effect of Indium Content on the Melting Point, Dross, and Oxidation Characteristics of Sn-2Ag-3Bi-XIn Solders. *J. Electron. Packag.* **2013**, *135*, 021006.
- (41) Miyake, I.; Tanpo, T.; Tatsuyama, C. XPS study on the oxidation of InSe. *Jpn. J. Appl. Phys., Part 1* **1984**, *23*, 172–178.
- (42) Donley, C.; Dunphy, D.; Paine, D.; Carter, C.; Nebesny, K.; Lee, P.; Alloway, D.; Armstrong, N. R. Characterization of Indium-Tin Oxide Interfaces Using X-Ray Photoelectron Spectroscopy and Redox Processes of a Chemisorbed Probe Molecule: Effect of Surface Pretreatment Conditions. *Langmuir* **2002**, *18*, 450–457.
- (43) Yu, P. Y.; Cardona, M. *Fundamentals of Semiconductors*; Springer, 1999.
- (44) Zhang, B. Y.; Liu, T.; Meng, B.; Li, X.; Liang, G.; Hu, X.; Wang, Q. J. Broadband High Photoresponse from Pure Monolayer Graphene Photodetector. *Nat. Commun.* **2013**, *4*, 1811.
- (45) Velusamy, D. B.; Kim, R. H.; Cha, S.; Huh, J.; Khazaeinezhad, R.; Kassani, S. H.; Song, G.; Cho, S. M.; Cho, S. H.; Hwang, I.; Lee, J.; Oh, K.; Choi, H.; Park, C. Flexible Transition Metal Dichalcogenide Nanosheets for Band-Selective Photodetection. *Nat. Commun.* **2015**, *6*, 8063.
- (46) Klee, V.; Preciado, E.; Barroso, D.; Nguyen, A. E.; Lee, C.; Erickson, K. J.; Triplett, M.; Davis, B.; Lu, I.-H.; Bobek, S.; McKinley, J.; Martinez, J. P.; Mann, J.; Talin, A. A.; Bartels, L.; Léonard, F. Superlinear Composition-Dependent Photocurrent in CVD-Grown Monolayer MoS₂(1-x)Se_{2x} Alloy Devices. *Nano Lett.* **2015**, *15*, 2612–2619.
- (47) Bera, K. P.; Haider, G.; Usman, M.; Roy, P. K.; Lin, H. I.; Liao, Y. M.; Inbaraj, C. R. P.; Liou, Y. R.; Kataria, M.; Lu, K. L.; Chen, Y.-F. Trapped Photons Induced Ultrahigh External Quantum Efficiency and Photoresponsivity in Hybrid Graphene/Metal-Organic Framework Broadband Wearable Photodetectors. *Adv. Funct. Mater.* **2018**, *28*, 1804802.
- (48) Muñoz, E.; Monroy, E.; Garrido, J. A.; Izpura, I.; Sánchez, F. J.; Sánchez-García, M. A.; Calleja, E.; Beaumont, B.; Gibart, P. Photoconductor gain mechanisms in GaN ultraviolet detectors. *Appl. Phys. Lett.* **1997**, *71*, 870–872.
- (49) Liu, L.; Yang, C.; Patané, A.; Yu, Z.; Yan, F.; Wang, K.; Lu, H.; Li, J.; Zhao, L. High-detectivity ultraviolet photodetectors based on laterally mesoporous GaN. *Nanoscale* **2017**, *9*, 8142–8148.
- (50) Huang, W.; Gan, L.; Yang, H.; Zhou, N.; Wang, R.; Wu, W.; Li, H.; Ma, Y.; Zeng, H.; Zhai, T. Controlled Synthesis of Ultrathin 2D β-In₂S₃ with Broadband Photoresponse by Chemical Vapor Deposition. *Adv. Funct. Mater.* **2017**, *27*, 1702448.
- (51) Mudd, G. W.; Svatek, S. A.; Hague, L.; Makarovskiy, O.; Kudrynskiy, Z. R.; Mellor, C. J.; Beton, P. H.; Eaves, L.; Novoselov, K. S.; Kovalyuk, Z. D.; Vdovin, E. E.; Marsden, A. J.; Wilson, N. R.; Patané, A. High Broad-Band Photoresponsivity of Mechanically Formed InSe–Graphene van der Waals Heterostructures. *Adv. Mater.* **2015**, *27*, 3760–3766.
- (52) Wu, F.; Xia, H.; Sun, H.; Zhang, J.; Gong, F.; Wang, Z.; Chen, L.; Wang, P.; Long, M.; Wu, X.; Wang, J.; Ren, W.; Chen, X.; Lu, W.; Hu, W. AsP/InSe Van der Waals Tunneling Heterojunctions with Ultrahigh Reverse Rectification Ratio and High Photosensitivity. *Adv. Funct. Mater.* **2019**, *29*, 1900314.
- (53) Zhou, X.; Hu, X.; Zhou, S.; Song, H.; Zhang, Q.; Pi, L.; Li, L.; Li, H.; Lü, J.; Zhai, T. Tunneling Diode Based on WSe₂/SnS₂ Heterostructure Incorporating High Detectivity and Responsivity. *Adv. Mater.* **2018**, *30*, 1703286.
- (54) Zhou, X.; Gan, L.; Tian, W.; Zhang, Q.; Jin, S.; Li, H.; Bando, Y.; Golberg, D.; Zhai, T. Ultrathin SnSe₂ Flakes Grown by Chemical Vapor Deposition for High-Performance Photodetectors. *Adv. Mater.* **2015**, *27*, 8035–8041.
- (55) Li, J.; Niu, L.; Zheng, Z.; Yan, F. Photosensitive Graphene Transistors. *Adv. Mater.* **2014**, *26*, 5239–5273.
- (56) Sun, Z.; Liu, Z.; Li, J.; Tai, G.-a.; Lau, S.-P.; Yan, F. Infrared Photodetectors Based on CVD-Grown Graphene and PbS Quantum Dots with Ultrahigh Responsivity. *Adv. Mater.* **2012**, *24*, 5878–5883.